Journal of Materials Chemistry A

ROYAL SOCIETY OF CHEMISTRY

PAPER

View Article Online
View Journal

Cite this: DOI: 10.1039/d6ta02142e

Side-arm sterics direct conformation, topology, and function in zirconium metal–organic frameworks

Haofan Yang, [a] Qianhui Wang,[a] Thang D. Pham,[b] Zhiwei Wang,[a] Haomiao Xie, [a] Yongjie Xu,[c] Filip Formalik, [bd] Davide M. Proserpio, [e] Charlotte L. Stern,[a] Alice Li,[a] Xavier C. Krull,[a] Andrew I. Cooper, [c] Randall Q. Snurr [b] and Joseph T. Hupp *[a]

While steric control of linker conformation has proven effective for accessing new Zr-MOF structures, existing strategies have largely relied on modification of the linker core—an approach that intrinsically couples steric effects to framework connectivity, limits available functionalization sites, and often requires complex synthesis, particularly for high-connectivity linkers. Here, we introduce a conceptually distinct and adaptable strategy for topological control based on steric modulation through side-arm functionalization, which enables independent steric tuning without altering linker connectivity while remaining synthetically simple. Six amide or cyano groups positioned on the ligand side arms act as unconventional steric units to induce isolable conformational variability. This design enables the linker to flex and twist, guiding the formation of two isostructural Zr-MOFs, AM-Zr-1 and CN-Zr-1, adopting the rare underlying net 6,8-c *nuh*1 (or 3,8-c *nuh*2) with highly distorted, topologically complex porous architectures. Despite their identical connectivity, AM-Zr-1 generates a geometrically unique amide pocket that enhances CO_2 binding and affords higher CO_2/N_2 and CO_2/CH_4 selectivity, whereas the less bulky cyano substituents confer a more extended conformation to CN-Zr-1, resulting in higher surface area and H_2 uptake. These findings highlight steric side-arm functionalization as a simple yet versatile strategy for tuning Zr-MOF topology and function.

Received 11th March 2026
Accepted 27th March 2026

DOI: 10.1039/d6ta02142e

rsc.li/materials-a

Introduction

Metal–organic frameworks (MOFs) are designable porous crystalline materials constructed from metal-containing "nodes" and multitopic organic "linkers".[1,2] Zirconium MOFs featuring oxy-anion-terminated linkers are of substantial interest due to: (a) their high stability, deriving from strong Zr–O coordination bonds, (b) the preference of Zr(IV) for coordination of eight atoms, and (c) their propensity to form hexa-zirconium/oxy node cores that can connect to as many twelve chelating or bridging linkers and nonstructural ligands.[3,4] Since the first synthesis of a Zr-MOF in 2008 (UiO-66),[5] many successful efforts have been made to develop examples exhibiting ample & broad structural diversity, outstanding chemical stability, and intriguing functional properties.[3,6–10] Nevertheless, discovery of new structures that exploit new topologies is desirable and, indeed, essential for extending, expanding, and enhancing potential applications and for deepening our collective understanding of fundamental correlations between framework structure and properties.[11]

The topological and structural features of MOFs are typically defined and controlled by the geometry and coordination number of the selected metal nodes and organic linkers.[11] However, arbitrariness of metal node formation under various MOF synthetic conditions can induce uncertainty for accessing an expected topology with a desired application. On the other hand, most organic linkers are normally robust in the MOF formation procedure, and more importantly, the geometry and chemical structure of linkers can be well-controlled by various cross-coupling reactions.[12] Therefore, rational design of organic linkers is critical to expanding the diversity of MOF topologies and for modifying the functionality of MOFs with targeted properties and applications.[11,13]

Steric control over linker conformation holds great potential to enhance the structural and topological diversity of highly connected Zr-MOFs. For example, the introduction of steric hindrance by bulky substituents on the 2- and 2′-positions of a ditopic linker (biphenyl-4,4′-dicarboxylate (BPDC)) forces the

[a]Department of Chemistry, Northwestern University, Evanston, Illinois 60208, USA. E-mail: j-hupp@northwestern.edu

[b]Department of Chemical & Biological Engineering, Northwestern University, Evanston, Illinois 60208, USA

[c]Materials Innovation Factory & Department of Chemistry, University of Liverpool, 51 Oxford Street, Liverpool L7 3NY, UK

[d]Department of Micro, Nano, and Biomedical Engineering, Wroclaw University of Science and Technology, 50-370 Wroclaw, Poland

[e]Dipartimento di Chimica, Università degli studi di Milano, Via Golgi 19, 20133 Milano, Italy

two carboxylates and phenyl rings into a perpendicular configuration, leading to the formation of PCN-700 with an 8-connected **bcu** underlying net,[14,15] rather than UiO-67 with a 12-c **fcu** net.[5] Similarly, for tritopic linkers with the same D_{3h} symmetry, sterically assisted twisting of the three peripheral phenyl rings such that they become perpendicular to the central one in 1,3,5-benzenetribenzoate (BTB) results in the formation of a MOF with 3,8-c **the** net rather than one consisting of 2D 3,6-c **kgd** nets perpendicularly polycatenated.[16,17] Introduction of steric hindrance to tetratopic linkers has not only contributed to topology diversity but also has enhanced the stability of Zr-MOFs toward moisture due, in part, to ligand rigidification.[18] The strategies used for introducing steric hindrance usually focus on functionalizing the central core of the linker backbone,[18–23] and multi-step syntheses are often required to access these organic linkers with intricate geometry and chemical structure, especially for linkages with higher connectivity such as hexatopic linkers.[23,24] Higher connectivity is generally beneficial for topological diversity.[23,25] Moreover, the linker core typically offers only a limited number of functionalization sites, and modifications at the core can directly affect coordination geometry and connectivity. In contrast, side-arm functionalization introduces additional design handles while preserving core connectivity, providing greater flexibility for steric tuning and opportunities for post-synthetic modification.

Here, we present a new approach to steric control that introduces steric units on linker side arms by a facile and versatile strategy for tuning linker conformation and framework topology in Zr-MOFs. Briefly, we designed two conjugate acids of hexacarboxylated ligands: 4,4′,4″,4‴,4⁗,4⁗′-(benzene-1,3,5-triyltris(3,5-dicarbamoylpyridine-4,2,6-triyl))hexabenzoic acid (**H_6AM-BTP**) and 4,4′,4″,4‴,4⁗,4⁗′-(benzene-1,3,5-triyltris(3,5-dicyanopyridine-4,2,6-triyl))hexabenzoic acid (**H_6CN-BTP**). These ligands incorporate amide or cyano groups on the side arms to introduce steric hindrance and offer conformation flexibility (Fig. 1). This design leads to the formation of structurally complex 3D Zr-MOFs. The resulting frameworks, AM-Zr-1 (from **H_6AM-BTP**) and CN-Zr-1 (from **H_6CN-BTP**), adopt a 6,8-c *nuh*1 (or 3,8-c *nuh*2 underlying net), as calculated by ToposPro 5.5.3.1.[26,27] Despite sharing the same overall topology, AM-Zr-1 and CN-Zr-1 present different pore chemical environments and display different gas sorption behavior.

Results and discussion

H_6AM-BTP is a newly designed dendritic ligand featuring three chemically identical dicarbamoylpyridine (DCMP) arms and a central benzene core (Fig. 1b and 2a–d). Its structural analogue, **H_6CN-BTP**, incorporates three dicyanopyridine (DCNP) arms, differing only by replacement of the amide groups with cyano substituents (Fig. 1b and 2e–h). Despite their structural complexity, **H_6AM-BTP** and **H_6CN-BTP** were obtained *via* the modified Hantzsch pyridine synthesis from readily available aldehyde and β-keto nitriles precursors under metal-free conditions with straightforward purification (Fig. 1b). The ligands were subsequently characterized by ^{1}H, ^{13}C, and ^{1}H–^{15}N HSQC and HMBC NMR spectroscopy, as well as mass spectrometry (Fig. S1–8 and SI). Notably, the Hantzsch pyridine synthesis has been shown to be applicable to a wide range of aromatic aldehydes and β-keto nitrile derivatives;[28] this versatility is demonstrated here by employing commonly available aromatic aldehydes and β-keto nitrile derivatives to access the additional side-arm-functionalized molecules, which were characterized by NMR spectroscopy (Fig. 1b and S9–14).

To give insight into the steric tuning effect of the amide and cyano groups and the conformational dynamics of the molecules, relaxed energy scans of single (isolated) simplified models of the **H_6AM-BTP** and **H_6CN-BTP** molecules were computed using density functional theory (DFT) (in the simplified model, COOH groups were replaced with H atoms for computational efficiency). The highest energies of the simplified model of **H_6AM-BTP** were observed when the dihedral angle between the arm and the benzene core was approximately 12° and 192°, indicating that a planar conformation is not energetically favorable (Fig. 2i). The simplified models of **H_6CN-BTP** displayed a similar profile, with the highest energies near 176° and 356°, consistent with the steric constraints imposed by the cyano groups. Notably, the energy penalty associated with the cyano substituents is smaller than that of the amides (Fig. 2i), suggesting that the bulkier amides impose stronger steric hindrance, whereas the smaller cyano groups act as weaker steric-tuning elements, affording greater conformational flexibility. In contrast, an unsubstituted analogue lacking amide or cyano groups exhibited relatively low energies at planar conformations (Fig. 2i and S15), highlighting the role of side-arm functionality in enforcing molecular twisting. For comparison, we also examined Me-TDCPB, a previously reported dendritic linker with methyl substituents on the core (Fig. S16).[29] Although methyl groups provide some steric bias, a simplified model of **H_6AM-BTP** exhibits higher relative energies near planar geometries than does Me-TDCPB. These results demonstrate that amide and cyano groups on side arms can impose steric modulation, providing a powerful means of conformational control.

To gain further insight into molecular conformations, we obtained a single crystal of **H_6AM-BTP** (C1) from diffusion of ethyl ether into a dimethylacetamide (DMAC) solution. C1 crystallized in the triclinic space group $P\bar{1}$ (Fig. S17 and Table S1). The steric repulsion arising from the side-arm amide groups, as well as between the amide groups and the central benzene core, forces **H_6AM-BTP** to adopt a nonplanar structure (Fig. S17), consistent with the DFT calculation of a single **H_6AM-BTP** molecule. Although the three DCMP arms are crystallographically distinct, each rotates clockwise relative to the central benzene, adopting dihedral angles of 71–79°. In this structure, the terminal carboxylic acids of all three DCMP arms engage in hydrogen bonding with the central amide groups (Fig. S18–S22). This "terminal-to-central" assembly decreases pore size and volume for the crystalline molecular (linker) solid, resulting in a maximum pore diameter of 8.05 Å and a solvent-accessible volume of 61% per unit cell. Excluding solvent molecules, these hydrogen bonds give a 6-c **pcu** supramolecular network. A second crystalline form (C2) was obtained from a hexane/acetic acid mixture (Fig. 2a–d, S21, and Table S1). Also

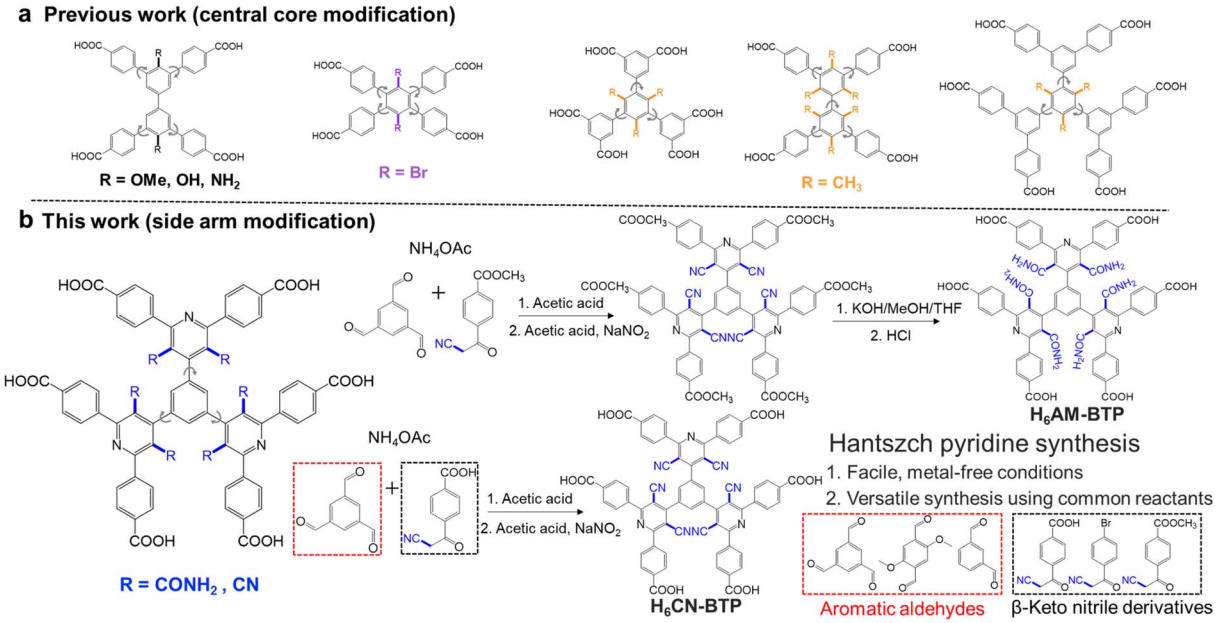

Fig. 1 Molecular structural control of conjugate acids of candidate carboxylate linkers by introducing steric hindrance at (a) the aromatic core and (b) the side arms. The reaction scheme illustrates the Hantzsch pyridine synthesis employed to construct the side-arm-functionalized linkers.

crystallizing in $P\bar{1}$, C2 retains some conformational features of C1 but displays a distinct arrangement of hydrogen-bonds. The DCMP arms adopt dihedral angles of 60–86°. Two arms participate in the same "terminal-to-central" assembly seen in C1 (Fig. 2j and S22), while the third engages in "terminal-to-terminal" carboxylic acid···carboxylic acid hydrogen bonding, which locally expands the pore. However, the expansion is counterbalanced by dense "central-to-central" amide···amide hydrogen bonding between neighboring molecules, ultimately reducing both the pore volume (40.7%) and the maximum pore diameter (6.38 Å). The overall hydrogen-bonded supramolecular network is built from a highly distorted 6-coordinated geometry, resulting in a rare kind of net called **bcu-x**-6-*C*2/*m*.[30]

We next obtained a single crystal of **H_6CN-BTP** (C3) from diffusion of hexane into an acetic acid solution. C3 crystallized in the triclinic space group $P\bar{1}$ (Fig. 2e–h, S23, and Table S1). Steric repulsion between the cyano substituents and the benzene core similarly enforces a twisted, nonplanar geometry, again consistent with DFT results and analogous to that observed for **H_6AM-BTP**. The three DCNP arms adopt dihedral angles of 61–85°. These results confirm that both amide and cyano groups on side arms function as steric tuning groups, driving molecular twisting away from planarity. C3 exhibited pore-expanding "terminal-to-terminal" carboxylic acid··· carboxylic acid hydrogen bonding (Fig. S24), but also exhibited pore-contracting dense π–π stacking interactions involving benzene···benzene and pyridine···pyridine pairs (Fig. 2k and S25), yielding a maximum pore diameter of 4.52 Å and a solvent-accessible volume of 31.4% per unit cell. By contrast, no π stacking is observed in C1 or C2, likely because the sterically demanding amides at the molecular center block close aromatic contacts. C1–C3 are all solvates, with carboxylic acid groups engaged in hydrogen bonding to solvent molecules. To expand pore size and volume, we aim to coordinate carboxylates with metal ions, a strategy that simultaneously frees the amide and cyano groups and makes them more accessible.

Solvothermal reaction of $ZrCl_4$ with **H_6AM-BTP** in the presence of formic acid as a competing reagent ("modulator") in *N*,*N*-diethylformamide (DEF) at 120 °C for 3 days afforded plate-like crystals of AM-Zr-1 (C4) of suitable size for single-crystal X-ray diffraction (SCXRD) analysis (Fig. 3a, b, and Table S1). AM-Zr-1 crystallizes in the orthorhombic space group *Pbam* with the formula $[(Zr_6O_4)_3(OH)_{12}(COO)_{12}(\text{AM-BTP})_4]$. The total solvent-accessible volume in the AM-Zr-1 framework is estimated to be 71% of its unit-cell volume. The combination of cubic 8-connected Zr_6 SBU and 6-connected trigonal-prismatic organic ligand gives rise to a highly distorted framework architecture. Following the guidelines from ToposPro,[26,27] in a single node cluster description, the structure can be simplified as 6,8-c tetranodal net with point symbol $(4^{11}\cdot6^4)_2(4^{13}\cdot6^2)_2(4^{20}\cdot6^8)_3$ (named *nuh*1) (Fig. S26 and S27). When using the all-node cluster description that considers the multibranched nature of the ligand, the framework, now called *nuh*2, is a 10-nodal 3,8-c net with point symbol $(4\cdot8^2)_{12}(4^{12}\cdot8^8\cdot10^8)_3(8^3)_4$ (Fig. 3c), where each of the two distinct ligands are now mapped on four 3-c nodes. The two nets were deposited by us last year in the TopCryst database.[31] The *nuh* topology has been reported in the peer-reviewed literature only very recently.[32] Its rarity likely arises from the limited availability of highly flexible trigonal-prismatic organic ligands, such as AM-BTP^{6-} and CN-BTP^{6-} in this work and the recently reported BTCH.[32]

Indicative of high flexibility for AM-BTP^{6-}, the unit cell of C4 contains two conformers. In both, the DCMP arms of coordinated AM-BTP^{6-} tilt nearly perpendicularly to the connected benzene core, adopting average dihedral angles of 88.3° and 87.1°, respectively, *i.e.* larger than those in C1 and C2 (Fig. 3d,

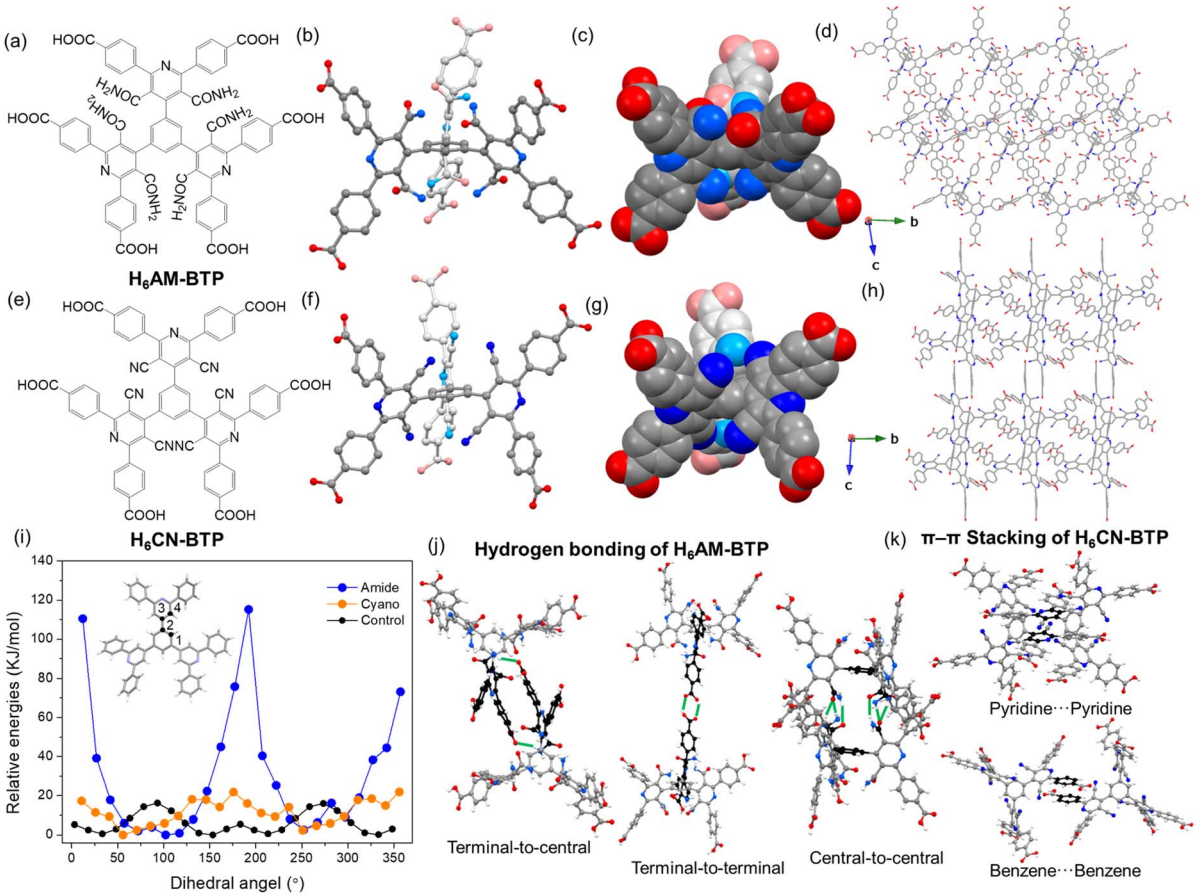

Fig. 2 (a) Chemical structure of H_6AM-BTP. (b and c) Ball/stick and space-filling representations of H_6AM-BTP extracted from single-crystal structure of C2. (d) Crystal-packing of C2 viewed from the *a* direction. (e) Chemical structure of H_6CN-BTP. (f and g) Ball/stick and space-filling representations of H_6CN-BTP extracted from single-crystal structure of C3. (h) Crystal-packing of C3 viewed from the *a* direction. (i) Relaxed energy scan of a simplified model of the H_6AM-BTP, H_6CN-BTP, and a control molecule without steric tuning on side arms performed at the M06-L + D3/Def2-TZVP level of theory (details in the SI, Section S3). The dihedral angle is defined by atoms 1-2-3-4 and screened every 15° as illustrated for the control molecule in the inset. (j) Hydrogen bonding of H_6AM-BTP in C2. (k) Benzene···benzene and pyridine···pyridine π stacking of H_6CN-BTP in C3. C, grey and black; N, blue; O, red; H, white. The hydrogen bond is highlighted green, and solvent molecules are omitted for clarity.

S28, and S29). This difference is likely a result of geometry constraints of the connection between the Zr_6 cluster and the linkers to match the *nuh*2 net. In addition, the geometry of the sp^2 carbons within the DCMP arms deviates from ideal hybridization, leading to carboxylate O atoms being displaced by up to 0.61 Å out of the pyridine plane and to a large angle distortion index (ADI) for the three N···N···N (pyridine) angles (Fig. 3d). The larger out-of-plane displacement and ADI in C4 relative to C1 and C2 indicate additional network strain. These unique features result in the formation of highly distorted pores along the *c* direction. The pores define one large distorted hexagonal 1D channel and two small diamond-shaped 1D channels, with pore openings of 15.46, 10.56, and 11.72 Å, respectively (determined by the smallest distance between opposing DCMP pyridine centroids) (Fig. 3e). To visualize the channels, we implemented an algorithm for pore network compartmentalization using the pyCOSMOS software (Fig. 3f, g, S30, and S31).[33] The 1D channels are crossed by twinned trigonal $(Zr_6)_3$(AM-BTP)$_2$ and tetragonal $(Zr_6)_2$(AM-BTP)$_4$ bipyramid cages (transverse to *c* direction) (Fig. 3h, i, and S32). The separations between four neighboring pyridine centers in one of the Zr_2(AM-BTP)$_4$ cages are 9.76 and 11.09 Å, respectively. The distance between two centroids of Zr nodes is 17.73 Å (Fig. 3i).

A single crystal of the CN analogue (C5, CN-Zr-1) was obtained from $ZrCl_4$ and **H_6CN-BTP** in DMF using benzoic acid as the modulator (Fig. S33 and Table S1). C5 also crystallizes in *Pbam* with formula $[(Zr_6O_4)_3(OH)_{12}(C_6H_5COO)_{12}$(CN-BTP)$_4]$ and is isostructural with C4. Substitution of amide groups by cyano groups leaves the overall composition, connectivity, and topology unchanged. Similar to C4, the unit cell of C5 contains two conformers with average dihedral angles of 85.9° and 84.3° (Fig. 3c). However, the cell volume (in particular, length in *a* direction) is slightly larger in C5 (Fig. S33). Notably, the smaller out-of-plane displacement of the carboxylate O atoms and lower ADI values in C5 relative to C4 indicate less structural distortion within the linker. This reduced distortion correlates with the slightly larger unit cell and reflects a more extended

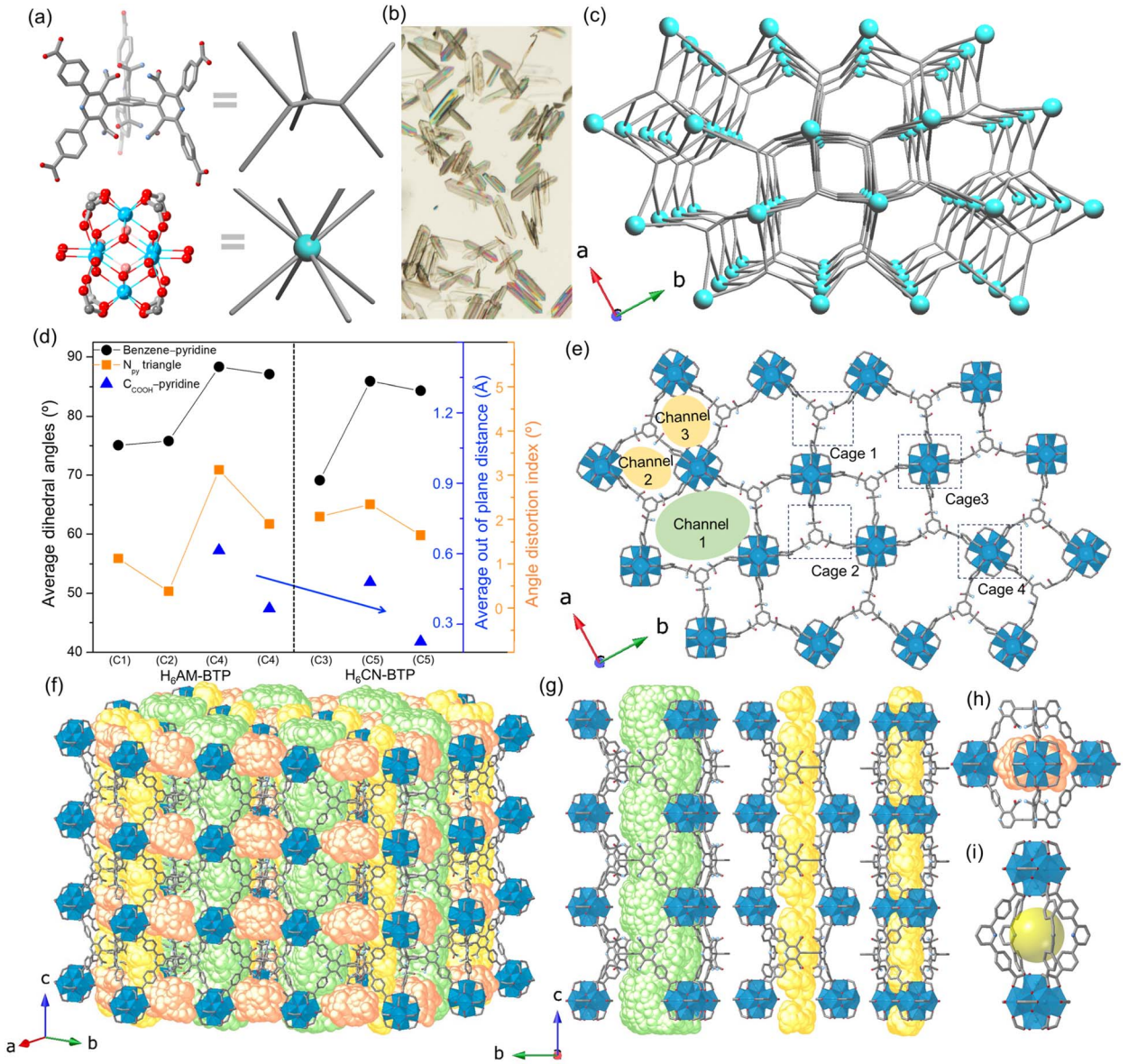

Fig. 3 (a) Zr_6 node and organic linker are simplified as blue dot and silver rod. (b) Optical image of single crystals of AM-Zr-1. (c) Underlying net of AM-Zr-1 (*nuh2*) generated by all-node cluster description using ToposPro software. (d) Average dihedral angle between the pyridine and the central benzene plane; angle distortion index (ADI), defined as the root-mean-square deviation of the three N···N···N (pyridine) angles from the ideal 60°; and the average out-of-plane displacement of the carboxylic acid O atoms relative to the pyridine plane, as determined from the crystal structures of C1–C5. (e) Crystal structure of AM-Zr-1 viewed from *c* direction highlighting channel and cage structures. (f) Porosity structure of AM-Zr-1 evaluated by pyCOSMOS software.[33] (g) Distorted-hexagonal (channel 1) and two small diamond-shaped 1D channels (channel 2 and 3) along *c* direction. (h) $(Zr_6)_3(AM\text{-}BTP)_2$ trigonal bipyramid cage (cage 1) consisting of three Zr_6 nodes and two linkers. (i) $(Zr_6)_2(AM\text{-}BTP)_4$ tetragonal bipyramid cage (cage 3) consisting of two Zr_6 nodes and four DCMP arms of linkers. Atoms: grey, C; light blue, N; red, O; dark blue, Zr; H is omitted for clarity.

conformation of $CN\text{-}BTP^{6-}$ compared to $AM\text{-}BTP^{6-}$ (Fig. 3c), consistent with the reduced steric demand and greater conformational flexibility of the cyano substituents.

The phase purity and structure of AM-Zr-1 and CN-Zr-1 microcrystals synthesized from DMF and formic acid were inferred/confirmed by the agreement of the experimental and calculated powder X-ray diffraction (PXRD) patterns (Fig. 4a and b). To further validate bulk phase purity, we performed a structureless refinement (Le Bail) of the PXRD data against the single crystal model (Fig. S34 and S35), which suggests that the bulk powder is mainly a single-phase product. No obvious structure change of AM-Zr-1 was observed after various liquid solvent exchanges (Fig. 4a and S36), but thermal activation under vacuum led to loss of crystallinity. The flexible feature of $AM\text{-}BTP^{6-}$ imposes a challenge in AM-Zr-1 activation, *i.e.* solvent removal with preservation of porosity, but also engenders restoration of crystallinity when the framework is re-exposed to solvent (Fig. S37). By using a gentler activation method –

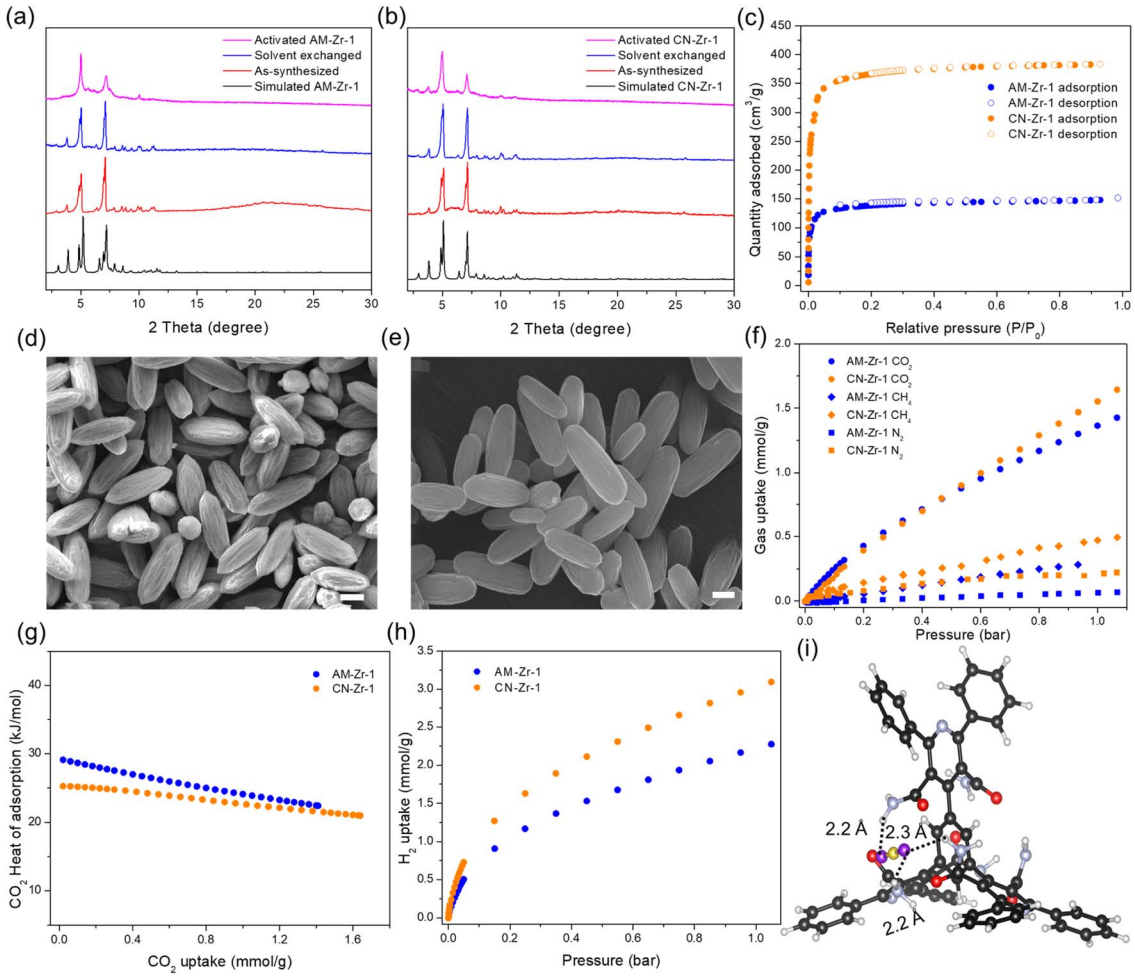

Fig. 4 (a) Simulated and experimental PXRD patterns of AM-Zr-1; experimental materials include SC-CO_2 activated, solvent exchanged with acetone, and as-synthesized samples. (b) Simulated and experimental PXRD patterns of CN-Zr-1. (c) N_2 adsorption–desorption isotherms at 77 K. (d and e) SEM image of activated (d) AM-Zr-1 and (e) CN-Zr-1 (scale bar = 1 μm). (f) Experimental adsorption isotherms of CO_2, CH_4, and N_2. (g) CO_2 adsorption enthalpies. (h) H_2 uptake at 77 K. (i) The lowest energy configurations of a CO_2 molecule interacting with the organic linker from DFT at the M06-L + D3/Def2-TZVP level of theory. Color code: H, white; C, black; N, light blue; O, red; C (CO_2), yellow; O (CO_2), purple.

supercritical carbon dioxide (SC-CO_2) drying[34–36] – activated AM-Zr-1 preserved crystallinity compared to as-synthesized states and CN-Zr-1 retains better crystallinity (Fig. 4a and b). The N_2 isotherm of activated samples showed a typical type I profile (Fig. 4c). CN-Zr-1 displayed a Brunauer–Emmett–Teller (BET) area of 1480 $m^2\ g^{-1}$, approximately 2.7 times higher than that of AM-Zr-1 (550 $m^2\ g^{-1}$). The larger BET of CN-Zr-1 is consistent with higher crystallinity after activation, and possibly because of more extended conformation for CN-BTP^{6-} (Fig. 4b). The measured surface area of CN-Zr-1 equates to 48.2% of the calculated nitrogen-accessible surface area, whereas that of AM-Zr-1 equates to only 20.7%, suggesting substantial pore collapse in the latter (Fig. S38). However, the structure can be recovered by heating collapsed AM-Zr-1 in DMF and formic acid (Fig. S39). Pore size distributions based on a nonlocal density functional theory (NLDFT) model indicated micropores with widths of 11.8 and 14.8 Å for both MOFs, though the total pore volume of CN-Zr-1 (0.51 $cm^2\ g^{-1}$) is much larger than that of AM-Zr-1 (0.19 $cm^2\ g^{-1}$) (Fig. S40). Both AM-Zr-1 and CN-Zr-1 retain their crystallinity after treatment with aqueous solutions of pH 1 HCl and pH 11 NaOH, as well as after boiling in water (Fig. S41). Thermogravimetric analysis (TGA) showed that both MOFs are stable up to 300 °C (Fig. S42). Fourier-transform infrared spectra confirmed the presence of amino groups in AM-Zr-1 and cyano groups in CN-Zr-1 (Fig. S43). Scanning electron microscopy revealed a prolate-shaped microrod morphology for activated AM-Zr-1 and CN-Zr-1 microcrystals with length of 2–4 μm and diameter of around 1 μm (Fig. 4d and e). Energy-dispersive X-ray spectroscopy (EDS) analysis performed on the selected region showed the presence of N-containing linker and Zr-containing node (Fig. S44 and S45). The ^{1}H NMR spectrum of digested AM-Zr-1 showed that no further hydrolysis of amide groups on **H_6AM-BTP** occurs during MOF synthesis under acidic condition (Fig. S46). However, ~25% of **H_6CN-BTP** molecules underwent partial hydrolysis to amide during CN-Zr-1 microcrystals synthesis (formic acid as modulator) (Fig. S47 and S48). Hydrolysis of **H_6CN-BTP** was significantly suppressed when benzoic acid was used as modulator, as evidenced by the

digested ^{1}H NMR spectra of CN-Zr-1 single crystals (benzoic acid as modulator) (Fig. S49). Solvothermally generated formate ions (adventitious capping ligands (nonstructural ligands))[37] were also found: ~4 per node for activated AM-Zr-1 and ~3.7 per node for activated CN-Zr-1 (Fig. S50 and S51).

MOFs with polar amide groups can enhance CO_2 binding affinity and selectivity.[38–40] The high density of amide functional groups (six per linker) with the unique spatial arrangement (geometrically tight three-amide pocket, AM_3) in AM-Zr-1 motivated us to explore gas sorption selectivity for CO_2 *vs.* CH_4 and CO_2 *vs.* N_2. The (single component) CO_2 sorption isotherm of activated AM-Zr-1 showed an uptake of 0.43 mmol g^{-1} at 0.2 bar and 1.36 mmol g^{-1} at 1 bar at 298 K (Fig. 4f). The CO_2 uptake increased to 2.1 mmol g^{-1} at 1 bar at 278 K (Fig. S52). By contrast, AM-Zr-1 showed negligible N_2 uptake (0.065 mmol g^{-1} at 1 bar) and low CH_4 uptake (0.28 mmol g^{-1} at 0.93 bar) at 298 K, leading to IAST-predicted selectivities of 220 and 28 for CO_2/N_2 (15/85) and CO_2/CH_4 (50/50) mixtures, respectively, at 298 K and 1 bar (Fig. S53 and S54).

CN-Zr-1 showed comparable CO_2 uptake (0.39 mmol g^{-1} at 0.2 bar and 1.55 mmol g^{-1} at 1 bar at 298 K), but higher uptakes of N_2 (0.21 mmol g^{-1} at 1 bar) and CH_4 (0.45 mmol g^{-1} at 0.95 bar) relative to AM-Zr-1 (Fig. 4f and S52). Isosteric heats of adsorption for CO_2, calculated using the virial method, were 29 and 22 kJ mol^{-1} for AM-Zr-1 at gas uptakes of 0.02 and 1.41 mmol g^{-1}, respectively, consistently higher than those of CN-Zr-1 across the full loading range (25 kJ mol^{-1} at 0.02 mmol g^{-1}) (Fig. 4g and S55). The decrease of isosteric heat over the entire loading range implies gradual saturation of the strongest binding sites for CO_2. In contrast, the more extended conformation of CN-BTP^{6-} in CN-Zr-1 affords a more robust framework with higher surface area and pore volume. Consequently, CN-Zr-1 displayed greater H_2 uptake (3.09 mmol g^{-1}) than AM-Zr-1 (2.27 mmol g^{-1}) at 1 bar at 77 K (Fig. 4h).

Cluster DFT calculations were performed to model the interactions between a CO_2 molecule and the MOF (AM-Zr-1) (Fig. S56). Although a single CO_2 molecule showed a shorter distance to the Zr node than to the amide group (Fig. 4i and S57), in the latter location the CO_2 molecule interacts with the AM_3 pocket through multiple close interactions: O $(CO_2)\cdots$H (amide) distances of 2.2, 2.3, 2.2 Å; C $(CO_2)\cdots$O (amide) distances of 2.9, 2.8, 4.7 Å; and C $(CO_2)\cdots$N (amide) distances of 3.6, 3.5, 4.0 Å (Fig. 4i). These close interactions result in higher enthalpies of adsorption for the CO_2 molecule interacting with the amide pocket than the Zr node (−15 *versus* −13 kJ mol^{-1} at 298 K and 1 atm, respectively). Cluster models neglect the dispersion interactions between the CO_2 molecule and the framework atoms that are not represented in the cluster, which may account for the lower heat of adsorption compared to the experiment. However, additional periodic calculations show that the dispersion interaction between the CO_2 molecule and the neglected framework atoms is −24 kJ mol^{-1} (Fig. S58), leading to adsorption enthalpies of −39 kJ mol^{-1} for the AM_3 pocket and −37 kJ mol^{-1} for the Zr node, both of which align better (but still not exactly) with the experimental heats of adsorption. We speculate that partial pore collapse in experimental samples accounts for the differences with enthalpies from computational modeling of uncollapsed material.

Conclusions

We have demonstrated that steric modulation through side-arm functionalization represents a powerful and versatile design strategy in reticular chemistry. Incorporating amide or cyano substituents into side arms of dendritic hexacarboxylated linkers induces isolable conformational variability that directs the assembly of two isostructural Zr-MOFs, AM-Zr-1 and CN-Zr-1, both adopting the rare *nuh*1 and *nuh*2 topologies. We also found that these steric units modulate not only framework topology but also functional properties. The densely arranged steric units (amide groups) generate a geometrically unique binding pocket that enhances CO_2 affinity and selectivity. On the other hand, the less bulky steric units (cyano groups) yield a more relaxed framework conformation, affording higher surface area and H_2 uptake. These results establish side-arm steric control as a complementary alternative to core substitution for shaping MOF topology and function, providing a versatile route to frameworks with tailored adsorption properties and other applications in the future.

Author contributions

H. Y. designed the study and carried out the experimental work. Q. W. contributed to synthesis, discussion, characterization, and data analysis. Z. W., H. X., Y. X., and X. C. K. assisted with characterization and analysis. T. D. P. and F. F. performed the simulations. D. M. P. conducted the topology analysis. C. L. S. and A. L. determined the single-crystal structures. A. I. C., R. Q. S., and J. T. H. contributed to scientific discussion and supervised the research. J. T. H. supervised the overall project. All authors discussed the results and commented on the manuscript.

Conflicts of interest

R. Q. S. and J. T. H. have equity interests in NuMat Technologies, a company that commercializes MOFs.

Data availability

CCDC 2454893–2454895, 2486952, and 2504783 contain the supplementary crystallographic data for this paper.[41a–e]

The data that support the findings of this study are presented in the paper and the supplementary information (SI). Supplementary information is available. See DOI: https://doi.org/10.1039/d6ta02142e.

Acknowledgements

R. Q. S. and J. T. H. acknowledge financial support from the U.S. Department of Energy Office of Science, Basic Energy Sciences, Program for Separation Science (DE-FG02-08ER15967) and from

Northwestern University. This research used resources of the National Energy Research Scientific Computing Center, a DOE Office of Science User Facility supported by the Office of Science of the U.S. Department of Energy under Contract No. DE-AC02-05CH11231 using NERSC award BES-ERCAP0026793. This research was supported in part through the computational resources and staff contributions provided for the Quest high performance computing facility at Northwestern University which is jointly supported by the Office of the Provost, the Office for Research, and Northwestern University Information Technology. This work made use of the IMSERC Crystallography, MS and NMR facilities at Northwestern University, which has received support from the Soft and Hybrid Nanotechnology Experimental (SHyNE) Resource (RRID:SCR_017874), and Northwestern University. X. C. K. acknowledges partial support from the U.S. Department of Energy through the Office of Science Graduate Student Research (SCGSR) program. D. M. P. thanks Prof. Vladislav A. Blatov at the Samara Center for Theoretical Materials Science for providing the free ToposPro software (https://topospro.com).

References

1 L. E. Kreno, K. Leong, O. K. Farha, M. Allendorf, R. P. Van Duyne and J. T. Hupp, *Chem. Rev.*, 2012, **112**, 1105–1125.
2 H. Furukawa, K. E. Cordova, M. O'Keeffe and O. M. Yaghi, *Science*, 2013, **341**, 1230444.
3 Y. Bai, Y. Dou, L.-H. Xie, W. Rutledge, J.-R. Li and H.-C. Zhou, *Chem. Soc. Rev.*, 2016, **45**, 2327–2367.
4 S. Yuan, L. Feng, K. Wang, J. Pang, M. Bosch, C. Lollar, Y. Sun, J. Qin, X. Yang, P. Zhang, Q. Wang, L. Zou, Y. Zhang, L. Zhang, Y. Fang, J. Li and H.-C. Zhou, *Adv. Mater.*, 2018, **30**, 1704303.
5 J. H. Cavka, S. Jakobsen, U. Olsbye, N. Guillou, C. Lamberti, S. Bordiga and K. P. Lillerud, *J. Am. Chem. Soc.*, 2008, **130**, 13850–13851.
6 T. C. Wang, W. Bury, D. A. Gómez-Gualdrón, N. A. Vermeulen, J. E. Mondloch, P. Deria, K. Zhang, P. Z. Moghadam, A. A. Sarjeant, R. Q. Snurr, J. F. Stoddart, J. T. Hupp and O. K. Farha, *J. Am. Chem. Soc.*, 2015, **137**, 3585–3591.
7 B. Wang, P. Wang, L.-H. Xie, R.-B. Lin, J. Lv, J.-R. Li and B. Chen, *Nat. Commun.*, 2019, **10**, 3861.
8 C. Koschnick, M. W. Terban, R. Frison, M. Etter, F. A. Böhm, D. M. Proserpio, S. Krause, R. E. Dinnebier, S. Canossa and B. V. Lotsch, *J. Am. Chem. Soc.*, 2023, **145**, 10051–10060.
9 W. Gong, X. Chen, K. M. Fahy, J. Dong, Y. Liu, O. K. Farha and Y. Cui, *J. Am. Chem. Soc.*, 2023, **145**, 13869–13878.
10 W. Gong, X. Chen, W. Zhang, K. O. Kirlikovali, B. Nan, Z. Chen, R. Si, Y. Liu, O. K. Farha and Y. Cui, *J. Am. Chem. Soc.*, 2022, **144**, 3117–3126.
11 M. Li, D. Li, M. O'Keeffe and O. M. Yaghi, *Chem. Rev.*, 2014, **114**, 1343–1370.
12 D. Zhao, D. J. Timmons, D. Yuan and H.-C. Zhou, *Acc. Chem. Res.*, 2011, **44**, 123–133.
13 L. Feng, Y. Wang, K. Zhang, K. Y. Wang, W. Fan, X. Wang, J. A. Powell, B. Guo, F. Dai, L. Zhang, R. Wang, D. Sun and H.-C. Zhou, *Angew. Chem., Int. Ed.*, 2019, **58**, 16682–16690.
14 S. Yuan, Y.-P. Chen, J.-S. Qin, W. Lu, L. Zou, Q. Zhang, X. Wang, X. Sun and H.-C. Zhou, *J. Am. Chem. Soc.*, 2016, **138**, 8912–8919.
15 S. Yuan, W. Lu, Y.-P. Chen, Q. Zhang, T.-F. Liu, D. Feng, X. Wang, J. Qin and H.-C. Zhou, *J. Am. Chem. Soc.*, 2015, **137**, 3177–3180.
16 B. Wang, X.-L. Lv, D. Feng, L.-H. Xie, J. Zhang, M. Li, Y. Xie, J.-R. Li and H.-C. Zhou, *J. Am. Chem. Soc.*, 2016, **138**, 6204–6216.
17 R. Wang, Z. Wang, Y. Xu, F. Dai, L. Zhang and D. Sun, *Inorg. Chem.*, 2014, **53**, 7086–7088.
18 X.-L. Lv, S. Yuan, L.-H. Xie, H. F. Darke, Y. Chen, T. He, C. Dong, B. Wang, Y.-Z. Zhang, J.-R. Li and H.-C. Zhou, *J. Am. Chem. Soc.*, 2019, **141**, 10283–10293.
19 X. Song, Y. Wang, C. Wang, D. Wang, G. Zhuang, K. O. Kirlikovali, P. Li and O. K. Farha, *J. Am. Chem. Soc.*, 2022, **144**, 10663–10687.
20 J. Pang, S. Yuan, J. Qin, C. Liu, C. Lollar, M. Wu, D. Yuan, H.-C. Zhou and M. Hong, *J. Am. Chem. Soc.*, 2017, **139**, 16939–16945.
21 T. Y. Tai, F. Sha, X. Wang, X. Wang, K. Ma, K. O. Kirlikovali, S. Su, T. Islamoglu, S. Kato and O. K. Farha, *Angew. Chem., Int. Ed.*, 2022, **61**, e202209110.
22 X. Zhao, X. Wang, S. Wang, J. Dou, P. Cui, Z. Chen, D. Sun, X. Wang and D. Sun, *Cryst. Growth Des.*, 2012, **12**, 2736–2739.
23 Z. Chen, Ł. J. Weseliński, K. Adil, Y. Belmabkhout, A. Shkurenko, H. Jiang, P. M. Bhatt, V. Guillerm, E. Dauzon, D.-X. Xue, M. O'Keeffe and M. Eddaoudi, *J. Am. Chem. Soc.*, 2017, **139**, 3265–3274.
24 O. K. Farha, A. Özgür Yazaydın, I. Eryazici, C. D. Malliakas, B. G. Hauser, M. G. Kanatzidis, S. T. Nguyen, R. Q. Snurr and J. T. Hupp, *Nat. Chem.*, 2010, **2**, 944–948.
25 V. Guillerm, Ł. J. Weseliński, Y. Belmabkhout, A. J. Cairns, V. D'elia, Ł. Wojtas, K. Adil and M. Eddaoudi, *Nat. Chem.*, 2014, **6**, 673–680.
26 C. Bonneau, M. O'Keeffe, D. M. Proserpio, V. A. Blatov, S. R. Batten, S. A. Bourne, M. S. Lah, J.-G. Eon, S. T. Hyde, S. B. Wiggin and L. Öhrström, *Cryst. Growth Des.*, 2018, **18**, 3411–3418.
27 V. A. Blatov, A. P. Shevchenko and D. M. Proserpio, *Cryst. Growth Des.*, 2014, **14**, 3576–3586.
28 X. Li, Y. Che, L. Chen, T. Liu, K. Wang, L. Liu, H. Yang, E. O. Pyzer-Knapp and A. I. Cooper, *Nat. Chem.*, 2024, **16**, 1286–1294.
29 J. Jia, F. Sun, H. Ma, L. Wang, K. Cai, Z. Bian, L. Gao and G. Zhu, *J. Mater. Chem. A*, 2013, **1**, 10112–10115.
30 V. A. Blatov, *Acta Crystallogr., Sect. A: Found. Crystallogr.*, 2007, **63**, 329–343.
31 A. P. Shevchenko, A. A. Shabalin, I. Y. Karpukhin and V. A. Blatov, *Sci. Technol. Adv. Mater.: Methods*, 2022, **2**, 250–265.
32 X.-J. Kong, H. Xie, J. Liu, T. He, X. Wang, K. Wang, X. Tang, B. Hou, K. O. Kirlikovali, R. Q. Snurr and O. K. Farha, *J. Am. Chem. Soc.*, 2026, **148**, 3562–3569.

33 S. Parashar and A. V. Neimark, *J. Chem. Inf. Model.*, 2024, **64**, 3260–3268.
34 A. P. Nelson, O. K. Farha, K. L. Mulfort and J. T. Hupp, *J. Am. Chem. Soc.*, 2009, **131**, 458–460.
35 O. K. Farha and J. T. Hupp, *Acc. Chem. Res.*, 2010, **43**, 1166–1175.
36 Y.-S. Bae, K. L. Mulfort, H. Frost, P. Ryan, S. Punnathanam, L. J. Broadbelt, J. T. Hupp and R. Q. Snurr, *Langmuir*, 2008, **24**, 8592–8598.
37 Z. Lu, J. Liu, X. Zhang, Y. Liao, R. Wang, K. Zhang, J. Lyu, O. K. Farha and J. T. Hupp, *J. Am. Chem. Soc.*, 2020, **142**, 21110–21121.
38 B. Zheng, J. Bai, J. Duan, L. Wojtas and M. J. Zaworotko, *J. Am. Chem. Soc.*, 2011, **133**, 748–751.
39 C. Chen, M. Zhang, W. Zhang and J. Bai, *Inorg. Chem.*, 2019, **58**, 2729–2735.
40 X. Song, M. Zhang, C. Chen, J. Duan, W. Zhang, Y. Pan and J. Bai, *J. Am. Chem. Soc.*, 2019, **141**, 14539–14543.
41 (*a*) CCDC 2454893: Experimental Crystal Structure Determination, 2026, DOI: 10.5517/ccdc.csd.cc2ndj3q.; (*b*) CCDC 2454894: Experimental Crystal Structure Determination, 2026, DOI: 10.5517/ccdc.csd.cc2ndj4r; (*c*) CCDC 2454895: Experimental Crystal Structure Determination, 2026, DOI: 10.5517/ccdc.csd.cc2ndj5s; (*d*) CCDC 2486952: Experimental Crystal Structure Determination, 2026, DOI: 10.5517/ccdc.csd.cc2pgw8b; (*e*) CCDC 2504783: Experimental Crystal Structure Determination, 2026, DOI: 10.5517/ccdc.csd.cc2q2fgq.